

The impact of GMC collisions on the star formation rate

Glen H. Hunter^{1,2,3*}, Paul C. Clark³, Simon C. O. Glover¹, Ralf S. Klessen^{1,4}

¹Universität Heidelberg, Zentrum für Astronomie, Institut für Theoretische Astrophysik, Albert-Ueberle-Str. 2, 69120 Heidelberg, Germany

²SUPA, School of Physics & Astronomy, University of St Andrews, North Haugh, St Andrews, KY16 9SS, United Kingdom

³School of Physics and Astronomy, Queen's Buildings, The Parade, Cardiff University, Cardiff, CF24 3AA, United Kingdom

⁴Universität Heidelberg, Interdisziplinäres Zentrum für Wissenschaftliches Rechnen, Im Neuenheimer Feld 205, 69120 Heidelberg, Germany

Accepted XXX. Received YYY; in original form ZZZ

ABSTRACT

We simulate the collision of two Giant Molecular Clouds (GMCs) using the moving mesh magnetohydrodynamical (MHD) code AREPO. We perform a small parameter space study on how GMC collisions affect the star formation rate (SFR). The parameters we consider are relative velocity, magnetic field inclination and simulation resolution. From the collisional velocity study we find that a faster collision causes star formation to trigger earlier, however, the overall trend in star formation rate integrate through time is similar for all. This contradicts the claim that the SFR significantly increases as a result of a cloud collision. From varying the magnetic field inclination we conclude that the onset of star formation occurs sooner if the magnetic field is parallel to the collisional axis. Resolution tests suggests that higher resolution delays the onset of star formation due to the small scale turbulence being more resolved.

Key words: stars: formation – ISM: clouds – galaxies: ISM

1 INTRODUCTION

Giant molecular clouds (GMCs) are large regions of gravitationally bound gas that exist within galaxies. These clouds typically span 1–100 pc in size and contain on the order $\sim 10^4$ – $10^6 M_{\odot}$ of molecular gas, giving them typical hydrogen densities of $\sim 100 \text{ cm}^{-3}$ (Blitz 1993; Roman-Duval et al. 2010). GMCs have temperatures of ~ 10 – 30 K, a factor of 2–10 times lower than the temperature of the surrounding Cold Neutral Medium (CNM) component of the interstellar medium (ISM). Due to their low temperatures and molecular nature, the main observational tracers of GMC properties are dust continuum emission and molecular line emission (from e.g. CO/HCN/N₂H⁺), which are used to observe GMCs within the Milky Way as well as in nearby galaxies (Fukui et al. 1999; Dame et al. 2001; André et al. 2010; Leroy et al. 2021).

Embedded within these GMCs are cooler dense clumps, the more massive of which are often observed as Infrared Dark Cloud (IRDCs). These clumps are accepted to be the precursor to star formation (Tan et al. 2014) due to their temperatures of 10–20 K (Chira et al. 2013) and higher number densities of $n_{\text{H}_2} = 10^4$ – 10^6 cm^{-3} (Motte et al. 2018). Each clump will likely form a cluster of stars due to further fragmentation and their relatively large mass reservoir (10^2 – $10^5 M_{\odot}$) (Motte et al. 2018). Despite many observations of these clumps, the process by which these clumps form is not fully understood. Some theoretical models have been proposed that explain how a GMC can fragment and further collapse; such as turbulence (Krumholz & McKee 2005), stellar and supernova feed-

back (Wareing et al. 2017) and converging gas flows, i.e collisions (Scoville et al. 1986; Wu et al. 2017).

Numerical simulations of galactic disks have shown that GMC collisions are a recurring event due to the quasi-2D geometry of the distribution of dense molecular gas in most disk galaxies along with the differential rotation created by the gravitational potential of the galaxy (Tasker & Tan 2009). The period of these collisions is of the order of 20% of the orbital period of the clouds around the centre of the galaxy, assuming a flat rotation curve in the disk (Dobbs et al. 2015). This is supported by the many observations of cloud collisions found within the Milky Way; for instance, Fukui et al. (2021) identify ~ 50 GMCs that are candidates to be the product of cloud-cloud collisions (CCCs). However, collisions are not limited to the disks of galaxies. Cloud collisions have been observed in the Small and Large Magellanic Clouds (SMC and LMC) (Fukui et al. 2019; Tokuda et al. 2019; Neelamkodan et al. 2021) and theorised to occur with extreme collisional velocities in the centre of the Milky Way (Sormani et al. 2019). In the case of the SMC and LMC, these clouds collide as a result of large scale HI flows caused by the tidal interactions of these satellite galaxies (Fukui et al. 2017). As for the centre of the galaxy, Sormani et al. (2019) argues the gas flow caused by the galactic bar crashes into the Central Molecular Zone, a ring of molecular gas surrounding the Milky Way nucleus, providing the ideal conditions for clouds to collide.

A variety of GMC collision simulations have shown an enhancement of the star formation rate, in both non-identical GMC collisions (Habe & Ohta 1992) and identical GMC collisions (Wu et al. 2017). In the former, the collision of the smaller cloud with the larger cloud creates a cavity and compression layer in which densities are reached that are high enough for high-mass stars to

* E-mail: glen.hunter@uni-heidelberg.de

form. This is consistent with observations, for example of the Gum 11 cloud in the Carina Nebula Complex by [Fujita et al. 2021](#), where CO observations indicate the presence of colliding clouds with a cavity, and with a massive star, HD92206, in close proximity to the compressed layer.

Despite the many simulations available, there is little agreement on how much the star formation rate is increased by a cloud-cloud collision. Some authors find that the increase is around a factor of a few ([Tanvir & Dale 2020](#)) whilst others observe an order of magnitude increase ([Wu et al. 2017](#)). These differences arise due to differences in the range of physical processes included in the simulation (e.g. equilibrium or non-equilibrium chemistry, feedback, magnetic fields etc.), as well as differences in the algorithm used to form stars and the physical resolution of the simulations.

In this paper we recreate the collision of two spherical GMCs of *molecular* gas using similar initial conditions to the study by [Wu et al. \(2017\)](#). The simulations are used to investigate the star formation that would occur in such collision, with a focus on the star formation rate. We run a total of 9 simulations, determining which property impacts the star formation the most.

The structure of the paper as follows. In Section 2 we discuss the numerical approach taken, the initial conditions used for each simulation and how the star formation is implemented. In Section 3 we present our results from the simulation, with a focus on the structure of the GMC, the star formation rate and the virial parameter of the cloud. We conclude with a comparison of our results to other literature results in Section 4 and a summary of our findings in Section 5.

2 METHODOLOGY

2.1 Numerical magnetohydrodynamics

We make use of the AREPO moving mesh code to simulate the gas dynamics and star formation of colliding GMCs ([Springel 2010](#)). The code solves the equations of magnetohydrodynamics (MHD) ([Pakmor & Springel 2013](#)),

$$\frac{\partial \rho}{\partial t} + \nabla \cdot (\rho \mathbf{v}) = 0, \quad (1)$$

$$\frac{\partial \rho \mathbf{v}}{\partial t} + \nabla \cdot (\rho \mathbf{v} \otimes \mathbf{v} + p_{\text{tot}} \mathbb{1} + \mathbf{B} \otimes \mathbf{B}) = -\rho \nabla \Phi, \quad (2)$$

$$\frac{\partial \rho e}{\partial t} + \nabla \cdot [\mathbf{v}(\rho e + p_{\text{tot}}) - \mathbf{B}(\mathbf{v} \cdot \mathbf{B})] = \dot{Q} + \rho \frac{\partial \Phi}{\partial t}, \quad (3)$$

$$\frac{\partial \mathbf{B}}{\partial t} + \nabla \cdot (\mathbf{B} \otimes \mathbf{v} - \mathbf{v} \otimes \mathbf{B}) = 0, \quad (4)$$

where ρ , \mathbf{v} and \mathbf{B} are the density, velocity and magnetic field strength of a given cell. Here, $\mathbb{1}$ is the identity matrix. The total pressure is the sum of the thermal and magnetic pressures, $p_{\text{tot}} = p_{\text{gas}} + \frac{1}{2} |\mathbf{B}|^2$. The total energy per unit mass is $e = e_{\text{th}} + \frac{1}{2} \mathbf{v}^2 + \Phi + \frac{1}{2\rho} |\mathbf{B}|^2$, where e_{th} is the thermal energy per unit mass. An adiabatic equation of state is adopted where $p_{\text{gas}} = (\gamma - 1)\rho e_{\text{th}}$ with $\gamma = 5/3$. Heating and cooling of the gas due to chemical changes and radiative processes is accounted for with the term \dot{Q} , which is discussed in more detail in Section 2.2.

The equations are solved on a tessellated Voronoi mesh in which the mesh generating points are able to follow the gas flow using a Harten-Lax-van Leer discontinuity (HLLD) solver. This

allows AREPO to act as a quasi-Lagrangian MHD code. The Voronoi mesh is adaptive: cells can be refined or de-refined by adding or removing mesh-generating points, respectively. The divergence-free constraint on the magnetic field, $\nabla \cdot \mathbf{B} = 0$, is enforced by the using the MHD solver provided in AREPO ([Pakmor & Springel 2013](#)). Here, additional source terms are added to Equations 2-4 following the scheme introduced by [Powell et al. \(1999\)](#) combined with a hyperbolic Dedner cleaning ([Dedner et al. 2002](#)). This minimizes any effect that a diverging magnetic field may create. However, due to the discretization of the Voronoi mesh, small divergences may still be present.

The gravitational term is due to the self-gravitation of the gas and any sink particles present within the system (see below). AREPO solves Poisson's equation,

$$\nabla^2 \Phi = 4\pi G \rho, \quad (5)$$

via a tree-based algorithm similar to the one used in the GADGET-2 code ([Springel 2005](#)), where G is the gravitational constant. The algorithm treats each cell as if the mass is at a point in the centre of the cell with a degree of gravity softening. The softening length for the gas is adaptive and is given as $\epsilon_{\text{gas}} = 2r_{\text{cell}}$, where the r_{cell} is the radius of a sphere with the same volume as the Voronoi cell. The minimum softening length for both the gas and sink particles is 40.02 AU. Further information on sink particles will be discussed in Section 2.3.

2.2 Chemical network

For our simulations we make use of a modified version of the chemical network developed by [Gong et al. \(2017\)](#), which itself is an improved version of prior networks developed by [Nelson & Langer \(1999\)](#) and [Glover & Clark \(2012\)](#). It includes a simplified treatment of the chemistry of H, C, and O and allows us to follow the evolution of the abundances of the main low temperature gas coolants (CO, C, O, and C⁺) with high accuracy, but low computational cost. A comprehensive description of the network can be found in [Gong et al. \(2017\)](#), and full details of the modifications we have made to it are described in Appendix A. Radiative heating and cooling of the gas are modelled using a detailed atomic and molecular cooling function, most recently described in [Clark et al. \(2019\)](#).

To treat the effects of H₂, C and CO self-shielding as well as shielding by dust, we make use of the TREECOL algorithm ([Clark et al. 2012](#)). It uses information stored in the gravitational tree structure to compute a 4π steradian map of the column densities of each of these species plus dust around each Voronoi cell. These maps are then used to determine how the interstellar radiation field (ISRF) reaching the cell is attenuated by self-shielding and dust absorption.

In all of our simulations, we adopt elemental carbon and oxygen abundances given by [Sembach et al. \(2000\)](#). Following [Draine \(1978\)](#), we set the strength of the interstellar radiation field (ISRF) to $G_0 = 1.7$ in [Habing \(1968\)](#) units. Finally, we adopt a value of $\zeta_{\text{H}} = 3 \times 10^{-17} \text{ s}^{-1}$ for the cosmic ray ionisation rate of atomic hydrogen.

2.3 Star formation

To simulate star formation, we make use of sink particles (henceforth sinks) to represent forming star clusters. We follow the sink creation protocol outlined in [Tress et al. \(2020\)](#). To summarise, the following conditions must be satisfied in order for a sink to be created:

a) The cell must have a density greater than a threshold density $\rho_c = 1.991 \times 10^{-16} \text{ g cm}^{-3}$.

b) The gas flow within the accretion radius of the sink ($r_{\text{acc}} = 187 \text{ AU}$) must be converging. We ensure this by requiring convergence of both the velocity field ($\nabla \cdot \mathbf{v} < 0$) and the acceleration field ($\nabla \cdot \mathbf{a} < 0$).

c) The sink-forming region must be situated within a local minimum of the gravitational potential.

d) The cell must not lie within a distance $r < r_{\text{acc}}$ of an existing sink particle.

e) The region within r_{acc} must be gravitationally bound, i.e. $|E_{\text{grav}}| > 2(E_{\text{therm}} + E_{\text{kin}})$ where E_{grav} is the gravitational energy, and E_{therm} and E_{kin} are the thermal and kinetic energies, respectively.

If all of these criteria are met, the gas cell is converted into a sink that inherits its mass and momentum. This sink is able to interact gravitationally with the surrounding environment and is also able to accrete further gas onto itself. Any Voronoi cells with $\rho > \rho_c$ within a distance $r < r_{\text{acc}}$ of a sink are potentially eligible for accretion. However, gas is only accreted from the cell if it is gravitationally bound to the sink. Provided this is the case, enough gas is removed from the cell to reduce its density to ρ_c , although the total amount removed at each time-step is capped at 90% of the cell's initial mass, for reasons of numerical stability. Following the accretion, any properties of the cell that depend on its mass are updated. It should be noted that the sinks formed do not contribute to the magnetic field of the system (i.e. $|B_{\text{sink}}| = 0$).

2.4 Initial conditions

In this paper we adopt the initial conditions provided in Wu et al. (2017), which were motivated by observations of GMCs. The simulations are initialised within a $(128 \text{ pc})^3$ domain of molecular gas with a mean molecular weight $\mu = 2.33$ and a helium to hydrogen fraction of 0.1. Two spherical clouds of radius $R_{\text{GMC}} = 20 \text{ pc}$ are placed into the domain with their centres separated by $(x, y, z) = (2R_{\text{GMC}}, 0, b)$ where $b = 0.5R_{\text{GMC}}$ (see Figure 1). Each cloud is initialised with a mass of $M_{\text{GMC}} = 9.3 \times 10^4 M_{\odot}$ and an initial temperature of 15 K by randomly distributing 2 million particles uniformly, achieving an initial mass resolution of $0.0465 M_{\odot}$. This results in a hydrogen nucleon density of $n = 80.2 \text{ cm}^{-3}$ within the clouds. Surrounding the clouds is a region of warmer molecular gas with $n = 7.14 \text{ cm}^{-3}$ and a temperature of $T=150 \text{ K}$.

A uniform magnetic field of $|B| = 10 \mu\text{G}$ in magnitude is set across the whole domain of the simulation. This results in an Alfvén velocity of $v_A = 2.06 \text{ km s}^{-1}$ for each cloud and a mass-to-flux ratio that is 6 times greater than the critical value for both clouds (Glassgold & Langer 1974), making them magnetically supercritical. The angle θ is the magnetic field inclination from the x -axis in the x - y plane and is varied between simulations to investigate whether the orientation of the magnetic field affects the star formation rate. (see Table 1).

We give the two clouds initial velocities of $v = +v_{\text{rel}}/2$ and $v = -v_{\text{rel}}/2$ for the clouds starting at negative and positive x , respectively, so that they will later collide at a relative velocity $v = v_{\text{rel}}$. We carry out simulations with a range of different v_{rel} , so that we can investigate how different collision strengths impact the star formation rate. We also include one case where $v_{\text{rel}} = 0$ (simulation 2), to allow us to investigate what happens in the absence of a collision.¹

¹ Note that even in this case, the clouds will eventually collide due to

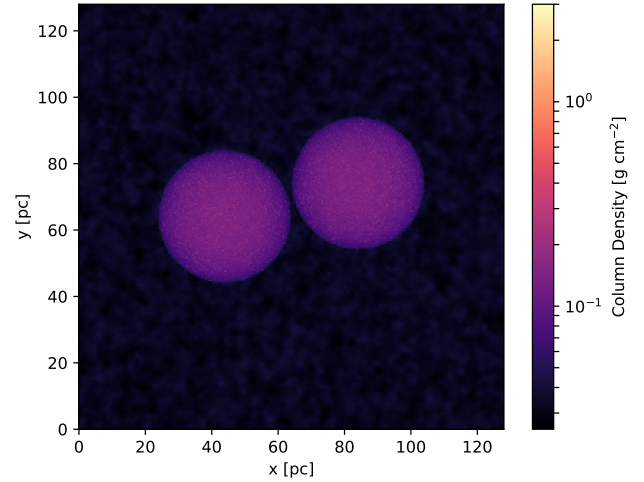


Figure 1. Surface density plot of the initial positions of the clouds.

Table 1. Initial conditions that are altered between simulations.

Simulation	θ ($^{\circ}$)	v_{rel} (km s^{-1})	Cells per Jeans length
1	60	10	8
2	60	0	8
3	60	5	8
4	60	15	8
5	0	10	8
6	30	10	8
7	90	10	8
8	60	10	4
9	60	10	16

Full details of the velocities used can be found in Table 1. Along with the collisional velocity, a turbulent velocity field is also applied to each cloud. The turbulence applied is purely solenoidal and has a 3D velocity dispersion of $\sigma = 3.46 \text{ km s}^{-1}$. This follows a scaling law of $P(k) \propto k^{-4}$. For the velocity field within each cloud the turbulence induced is both supersonic and super-Alfvénic, where $\mathcal{M} = \sigma/c_s = 11.6$ and $\mathcal{M}_A = \sigma/v_A = 1.68$ respectively.

We also investigate the effect of varying the number of cells per local Jeans length (hereafter referred to as the Jeans refinement parameter, JR). To do this we adopt Jeans refinement as our main cell refinement criterion in AREPO. Cells are refined by adding additional mesh generating points whenever $D > \lambda_J/\text{JR}$, where D is the effective diameter of the cell (i.e. the diameter of a sphere with the same volume as the mesh cell). We adopt $\text{JR} = 8$ as our default value for the Jeans parameter, but also investigate the behaviour of runs with $\text{JR} = 4$ and $\text{JR} = 16$, as detailed in Table 1.

3 RESULTS

3.1 Star formation rate

Each simulation results in a different progression of star formation. For an example, in Figure 2 it can be seen that the systems themselves

their mutual gravitational attraction. However, this will occur on a timescale $> 10 \text{ Myr}$, much longer than the period simulated here.

evolve differently, creating different structures. As a result, varying numbers of sink particles form in the different simulations, as shown in the figure. To investigate this difference quantitatively, we look at the star formation rate of each of the simulations.

The star formation rate is calculated as:

$$\dot{M}_{\text{SFR}} = \frac{\Delta M}{\Delta t} \quad (6)$$

where ΔM is the difference in the mass of the sinks between the start and end of a time step of length Δt . These are calculated for each output snapshot available in all nine simulations. The results from these calculations are presented in Figure 3 along with the total mass that has gone into star particles.

Figure 3 shows that there is a clear difference in the time taken for stars to begin forming in the different runs, with a spread in onset times of ~ 0.7 Myr between the most extreme cases. Looking in more detail at the results from the individual runs, we see that changing the collisional velocity has the greatest impact on the time required for star formation to begin. Stars start to form sooner in simulations with high collisional velocity than in simulations with low or zero collisional velocity. This behaviour is likely due both to the time it takes for large-scale shocks to form in the colliding clouds, and also to the density enhancement produced by these shocks. Faster collisions produce stronger shocks and hence larger density enhancements.² Therefore, higher density star-forming regions with shorter free-fall times are formed with increased collision velocity.

The orientation of the magnetic field has a smaller effect on the time required for star formation to begin. We see a clear difference in behaviour between the case with the magnetic field orientated parallel to the collisional axis, which forms stars after ~ 1.5 Myr, and the runs with other magnetic field orientations, in which the onset of star formation is delayed by ~ 0.25 Myr. The earlier star formation observed when the magnetic field is parallel to the collisional axis is a result of the magnetic field not hindering the compression of the gas along the x -axis. This allows the shocked gas to reach the densities required for the first sinks to be created more rapidly compared to the other magnetic field orientations (see also Appendix B).

Finally, regarding the Jeans refinement variation, a higher resolution tends to delay the onset of star formation. This is likely due to the higher resolved turbulence field resulting in more disruption to the star-forming gas. This results in the gas being unable to be fully bound, delaying star formation. However, it should be noted that the difference of the onset of star formation between the $JR = 8$ and $JR = 16$ cases is small, of the order of ~ 0.2 Myr, which is about the free-fall time of a dense core.

Figure 4 shows that the star formation rate in each simulation follows a similar trend from the point when sinks first form. For a brief period after the first sinks form, the SFR in the runs with $v_{\text{rel}} > 0$ is as much as an order of magnitude larger than in the run with $v_{\text{rel}} = 0 \text{ km s}^{-1}$, in which the clouds do not collide. However, the difference between the runs quickly decreases, and for the majority of the time covered by our simulations, the SFR in the cloud collision runs is only a factor of 2–3 larger than in the zero velocity run. This behaviour agrees to some extent with the claim made by Wu et al. (2017) that cloud collisions lead to an increase in the star formation rate. However, the magnitude of

the effect that we find here is much smaller than the consistent order of magnitude increase that they observed in their simulations, despite the similarity between our initial conditions and theirs. To investigate the origin of this difference in results, we look in the next section at the virial parameter of the clouds and clumps formed in the simulations.

3.2 Impact on the virial parameter

The virial parameter η provides an insight into how bound the star-forming region is by comparing the gravitational energy against all other energy contributions. We adapt the definition provided in Bertelli Motta et al. (2016) to include magnetic energy as a factor which counteracts gravitational collapse (Eqn. 7).

$$\eta = \frac{2(E_{\text{kin}} + E_{\text{therm}} + E_{\text{mag}})}{|E_{\text{grav}}|} \quad (7)$$

We chose to include the magnetic energy in this calculation as the gas we are considering is below sink formation threshold and does not exist near a sink. In order to make the comparison between the simulations we perform this analysis on the snapshot that was output ~ 1 Myr after the formation of the first sink particle. Note that this corresponds to a different physical time in each simulation, but should allow us to compare the clouds when they are at a similar stage in their evolution.

The regions used to determine the virial ratio are chosen by using the local minima of the potential. These are identified as part of the flux calculations within the MHD code and are stored within the outputs. After identification, we then compute the Jeans length for the gas located at the potential minimum. If a sink particle exists within 2 Jeans lengths of it, that minimum is no longer considered. We next select all gas cells lying within a single Jeans length of the identified minimum and compute the total gravitational, kinetic, magnetic and thermal energies of this set of gas cells. The gravitational energy, E_{grav} , is calculated via a direct N-body approach,

$$E_{\text{grav}} = - \sum_{i=1}^N \sum_{j=i+1}^N \frac{Gm_i m_j}{\Delta r_{ij}} \quad (8)$$

where m_i and m_j are the masses of the i th and j th cells, respectively, Δr_{ij} is the separation between the cells and N is the total number of cells within the selected region. The kinetic, magnetic and thermal energies, E_{kin} , E_{mag} and E_{therm} , are calculated as follows:

$$E_{\text{kin}} = \frac{1}{2} \sum_{i=1}^N m_i v_i^2, \quad (9)$$

$$E_{\text{mag}} = \frac{1}{8\pi} \sum_i |B_i|^2 \Delta V_i, \quad (10)$$

$$E_{\text{therm}} = \sum_i m_i e_{\text{th}_i}, \quad (11)$$

where m_i is the mass of cell i , v_i is the velocity of the cell relative to the potential minimum considered, $|B_i|$ is the magnetic field strength of the cell, $\Delta V_i = m_i/\rho_i$ is the approximate cell volume where ρ_i is the cell density, and e_{th_i} is the thermal energy per unit mass of the cell.

The number densities of associated with the local minima of the potential cover a wide range of values. For the purpose of this analysis we focus on a range of associated hydrogen nuclei number densities from $n = 100 \text{ cm}^{-3}$ to 10^6 cm^{-3} . Our motivation for

² Recall that for an isothermal shock, the strength of the density enhancement scales as the square of the Mach number. Although our model GMCs are not isothermal, the equilibrium temperature of the molecular gas varies only weakly with temperature, and so the isothermal result remains a useful guide.

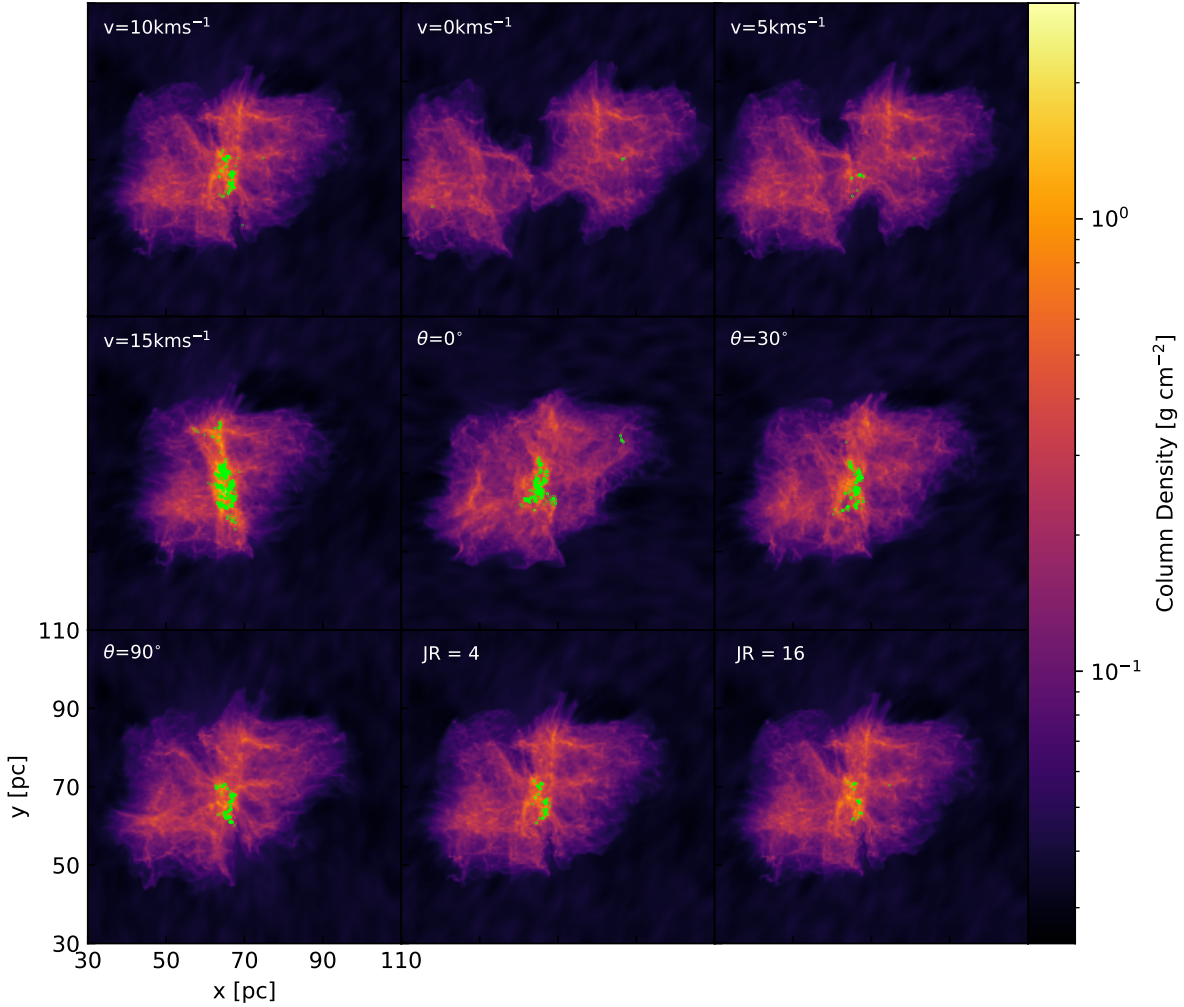


Figure 2. Column density plots of all simulations at $t = 2.40$ Myr. The green dots within the plot represent the sink particles that have formed.

adopting a lower limit of 100 cm^{-3} is to ensure that we are selecting regions associated with the cloud and not the surrounding intercloud medium. The upper limit is based on the sink formation criterion as discussed in Section 2.3, where, if a cell has a hydrogen nuclei number density greater than $n = 10^6 \text{ cm}^{-3}$, it can possibly form into a sink particle and remove mass from the surrounding gas. We split the data into bins of 10^k to 10^{k+1} cm^{-3} where $k = 2$ to $k = 5$ in integer steps.

In Figure 5, we show the ratio of each of the different components of the energy (thermal, magnetic, kinetic) to the gravitational energy as well as the averaged virial parameter for the hydrogen nuclei number density n bin considered for varying collisional velocity. The error bars indicate the range of values of each parameter in each bin.

Upon first inspection we note that the virial parameter is considerably greater than 1 in almost all of the regions we consider. This would imply that they are not gravitationally bound and thus would never form stars as a result. However, it should be noted we are considering only a single Jeans length from the potential minimum, and therefore we would expect to recover $\eta \sim 1$ for this region

even if the kinetic and magnetic energies were zero.³ Since these components are not zero, it is unsurprising that we recover $\eta \gg 1$ for most of these regions. In practice, all that this means is that the radius of the region that will ultimately collapse is greater than a single Jeans length, owing to the additional support provided by the turbulent motions and the magnetic field.

For the purposes of the comparison we are making here, we look for differences in the parameters between the simulations considered, and in particular for any general trends. For the ratio of E_{therm} to E_{grav} , we do not see a clear trend with collision velocity: the ratio increases with increasing v_{rel} in some density bins, but decreases or remains constant in other density bins. However, we observe a consistent increase in the ratios of E_{mag} to E_{grav} and E_{kin} to E_{grav} with increasing v_{rel} in all density bins. This is then reflected in the behaviour of the virial parameter, which also increases with increasing v_{rel} at all densities. This behaviour is a consequence of an increase in the turbulent motion of the dense molecular gas as the clouds collide with higher velocities. This directly increases the kinetic energy, but also results in additional tangling of the mag-

³ We do not recover exactly one because the density and temperature are not constant within the selected region.

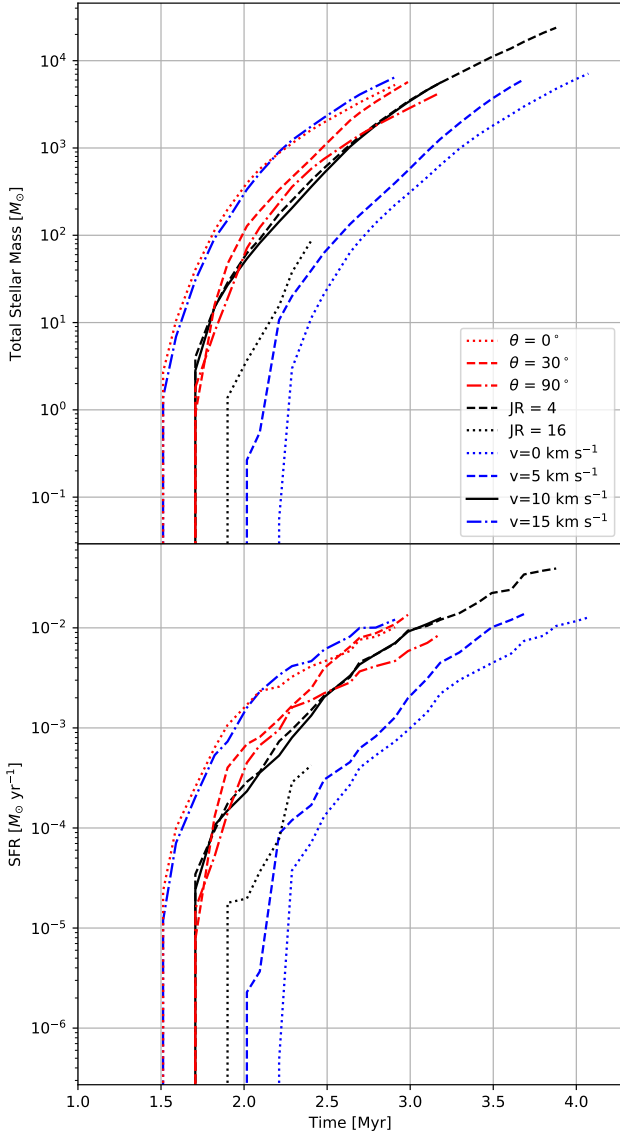


Figure 3. *Top:* Evolution of the mass in sink particles as a function of time in all nine simulations. *Bottom:* Star formation rate as a function of time in all nine simulations.

netic field, which increases the magnetic field strength and magnetic energy. These motions generally act against gravitational collapse and as a result fewer regions become gravitationally bound and star-forming, leading to a smaller increase in SFR than anticipated by Wu et al. (2017).

We have repeated the same analysis for the simulations with differing initial magnetic field inclinations (Fig. 6). Once again, we find that the ratio of E_{therm} to E_{grav} is substantially less than one in our lowest density bin and of order unity in the other bins. In the lowest density bin, we also observe a decrease in the average value of this ratio with increasing inclination angle. A reason for this could be that the gravitational energy calculated for these densities in the $\theta = 0^\circ$ simulation is higher due to compactness. The regions considered for this density bin exist on the outer parts of the clouds and visual inspection of the density maps shows more ‘flaring’ at the edges for greater magnetic field inclinations than for $\theta = 0^\circ$ (see also Figures B1 and B2). We see no clear trend in the value of the

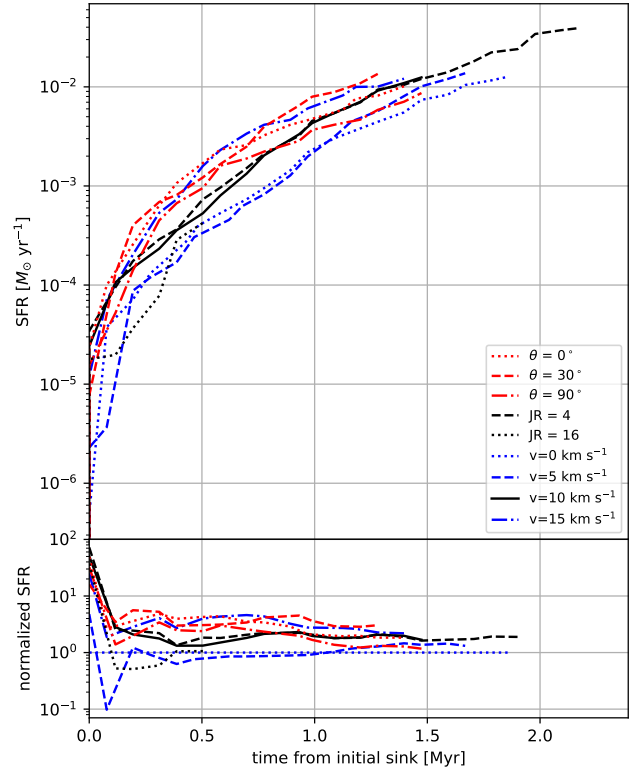


Figure 4. *Top:* Star formation rate varying with time from initial sink formation for all simulations. *Bottom:* Star formation rate normalised to $v_{\text{rel}} = 0$ km s $^{-1}$ star formation rate as a function of time from initial sink formation.

ratio with magnetic field inclination angle in the other density bins. The magnetic and kinetic to gravitational energy ratios, we find the values of these ratios to be similar across the different inclinations within a given density bin, thus in turn results in the virial ratio being constant across all magnetic field orientations for each density bin.

4 DISCUSSION

4.1 Comparison with Wu et al. (2017)

Our simulations demonstrate that rapid collisions between clouds lead to an earlier onset of star formation than in clouds that collide slowly or not at all. However, the way in which star formation proceeds once the process has set in is remarkably similar in all of our simulations. Note we find a persistent enhancement of a factor of 2–3 in the star formation rate in our colliding clouds compared to our $v = 0$ control run. The earlier onset of star formation and the increase in the star formation rate due to the collision are similar to the results reported by Wu et al. (2017) for very similar initial conditions. Contrary to Wu et al. (2017), we find a only a very weak departure of the SFR on the collision strength, i.e. on the collisional velocity, v_{rel} .

It is worthwhile considering possible methodological reasons for this difference. Aside from our use of a different magnetohydrodynamical code (Wu et al. use ENZO, we use AREPO), our simulations differ from those of Wu et al. (2017) in two main respects: our star formation algorithm and our treatment of chemistry and cooling.

In our simulations we make use of sink particles as our representation of stars or star clusters which are able to continue accreting

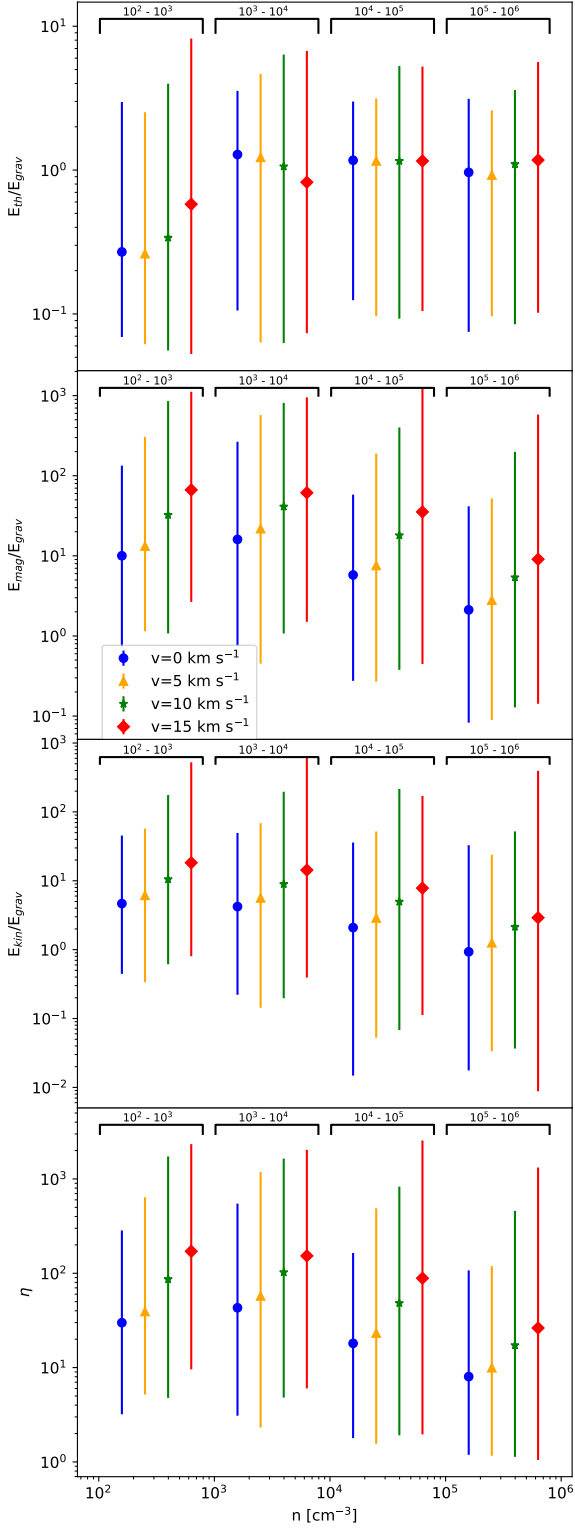


Figure 5. From the top down: The average a) thermal to gravitational energy ratio, b) magnetic to gravitational energy ratio, c) kinetic to gravitational energy ratio, and d) virial parameter for different collisional velocities v_{rel} . The error bars indicate the range of values obtained. Each density bin is indicated with the corresponding bracket annotation with the separation of the points for ease of reading. The points within a bracket are for the same density bin but are offset in the figure for clarity.

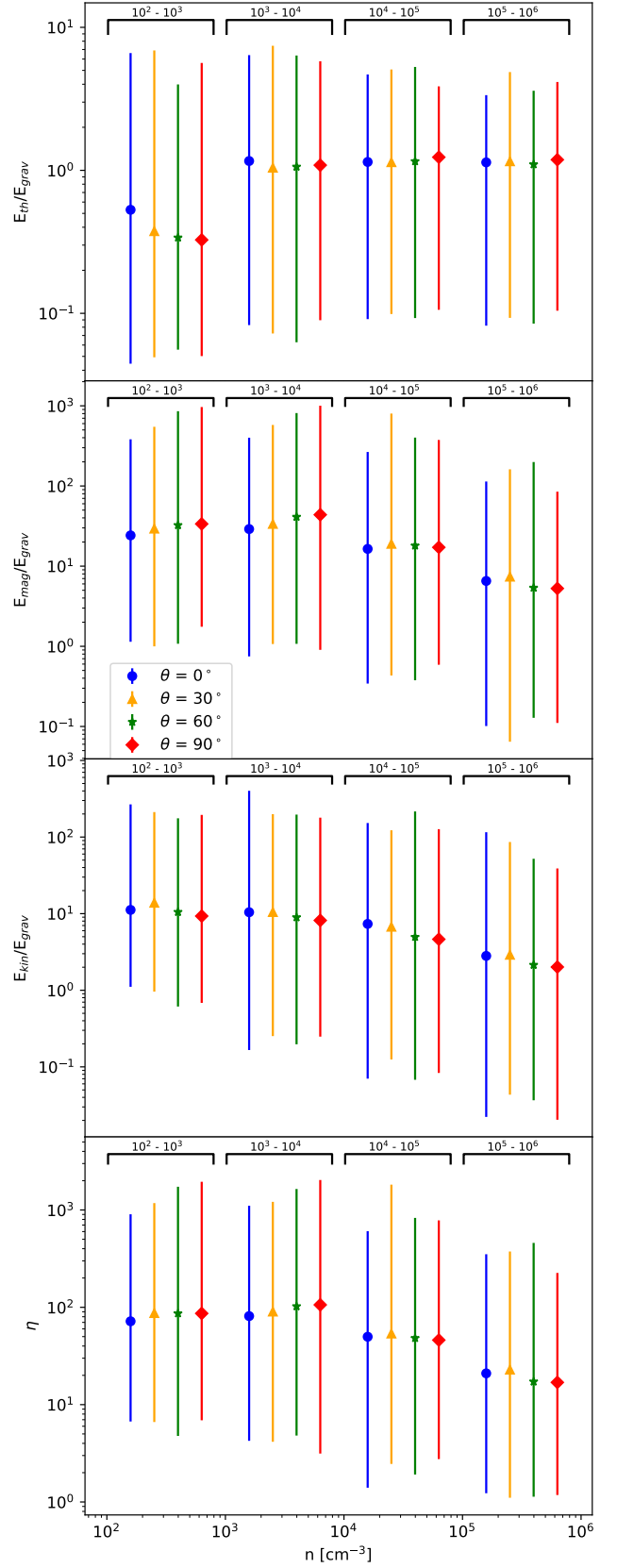


Figure 6. Same as figure 5 but looking at the differences in the inclination of magnetic field

after forming (see Sect 2.3). In contrast, [Wu et al. \(2017\)](#) make use of star particles that are formed stochastically with a fixed efficiency per free-fall time in gas cells on the finest level of refinement in their simulation that satisfy a suitably chosen criterion. In their “density-regulated” models, this criterion is a simple density threshold: star formation is permitted only in gas denser than $n_{\text{th}} = 10^6 \text{ cm}^{-3}$. In their “magnetically-regulated” models, on the other hand, star formation is permitted only in cells that are magnetically supercritical. Notably, they do not require the gas flow to be converging or the gas to be gravitationally bound in order for it to be eligible to form stars. A final difference between the treatment of star formation in the two approaches is that the star particles formed in the [Wu et al. \(2017\)](#) simulations have a fixed mass from the moment that they form, whereas our sink particles can continue to accrete mass as they age. [Wu et al. \(2017\)](#) argue that fixing the star particle mass is a way of approximately accounting for the effects of stellar feedback, and so logically simulations without this restriction should form a greater number of stars. However, comparison between our runs and those of [Wu et al. \(2017\)](#) shows that we actually recover much lower star formation rates, by around an order of magnitude.

The simplest explanation for the difference between our study and the results of [Wu et al. \(2017\)](#) is the different star formation criteria applied in the two approaches. [Wu et al. \(2017\)](#) motivate their adoption of a simple density or mass-to-flux ratio threshold on the grounds of the limited resolution of their simulations (smallest cell size $\Delta x = 0.125 \text{ pc}$), which does not make them confident that they can resolve the small scale structure of the gas well enough to apply a more complicated criterion. Our spatial resolution is much better in gravitationally collapsing regions, thanks to the Jeans refinement criterion, with our minimum cell size becoming as small as $\sim 10^{-4} \text{ pc}$ shortly before sink particle formation. We therefore do a much better job of resolving the structure of the dense gas and can easily distinguish between dense gas that is gravitationally bound and star-forming and dense gas that is not gravitationally bound. As a result, we recover much smaller star formation rates than in the [Wu et al. \(2017\)](#) simulations. For example, in our non-collisional ($v_{\text{rel}} = 0$) case we form $\sim 100 M_{\odot}$ worth of sinks over the first $\sim 0.5 \text{ Myr}$ of star formation, while [Wu et al. \(2017\)](#) form on the order of $\sim 1000 M_{\odot}$ worth of stars in a similar time frame in their $v = 0$ runs.

Although we consider the difference in the star formation algorithm to be the most likely cause of the difference between our results and those of [Wu et al. \(2017\)](#), it is worthwhile examining whether the difference in our chemical and thermal treatment may also play a role here. As previously mentioned, in our simulations, we use a modified version of the [Gong et al. \(2017\)](#) chemical network, together with the atomic and molecular cooling function described in [Clark et al. \(2019\)](#). On the other hand, [Wu et al. \(2017\)](#) make use of the GRACKLE library ([Smith et al. 2017](#)). The chemical networks provided in GRACKLE allow one to model the non-equilibrium chemistry of hydrogen (including H_2 formation and destruction), but do not account for the chemistry of metals such as carbon or oxygen. To account for heating and cooling due to metals, GRACKLE uses a table-based approach: the relevant rates are interpolated from a set of tables in which the rates are given as a function of density, temperature and (optionally) metallicity. GRACKLE includes several sets of tables computed using the CLOUDY photodissociation region (PDR) code ([Ferland et al. 1998](#)), but also allows the user to supply their own. [Wu et al. \(2017\)](#) make use of this latter option, using a set of cooling tables generated by [Wu et al. \(2015\)](#) using the PyPDR code ([Bruderer 2019](#)).

The impact of this difference in approach can be seen if we

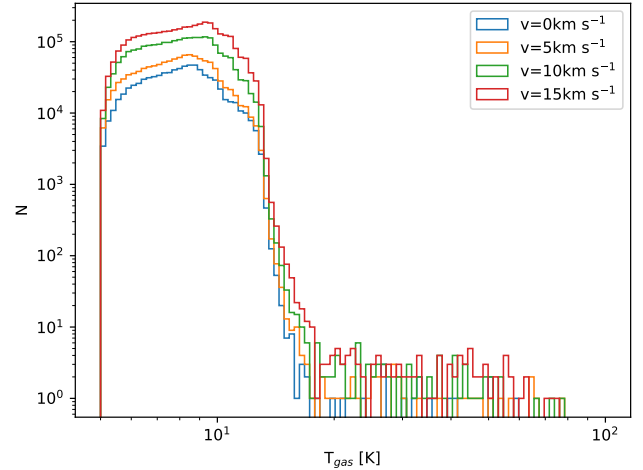


Figure 7. Temperature distribution of all gas cells of $n \geq 10^5 \text{ cm}^{-3}$ for different collisional velocities

compare the temperature distribution of the dense gas in our simulations (shown in Figure 7) with the temperature distribution of the star-forming gas in the [Wu et al. \(2017\)](#) simulations (shown in their figure 6). We find that most of the dense gas in our simulations has a temperature in the range $5 < T < 20 \text{ K}$, with a small tail in the distribution extending up to $\sim 100 \text{ K}$. We also find that there is no clear difference in the temperature distribution of the dense gas in between the colliding and the $v = 0$ runs. On the other hand, [Wu et al. \(2017\)](#) recover a somewhat broader temperature distribution, covering the range $10 < T < 40 \text{ K}$ in their non-colliding runs and extending up to $\sim 100 \text{ K}$ in the colliding runs. This broader temperature distribution may be a consequence of the stronger UV field adopted in their calculation – they assume $G_0 = 4$, compared to $G_0 = 1.7$ here – or may be due to some other aspect of the way in which cooling is treated in the two sets of simulations. Whatever the reason, it is clear that the difference in temperature distributions cannot explain the different star formation rates recovered in the simulations: there is an aspect of scale involved as well. When clouds collide at higher temperatures larger structures are able to form and collapse faster due to higher sound speeds present. However, due to higher Mach numbers, collisions are not as efficient at forming dense regions. For us, our dense gas is colder on average than that in the [Wu et al. \(2017\)](#) models and hence has less thermal support, meaning that it should be more likely to form dense regions and then stars, rather than less likely.

4.2 Do cloud collisions trigger star formation?

There is growing observational evidence, summarized recently by [Fukui et al. \(2021\)](#), that the formation of massive stars is often associated with molecular clouds that show signs of having undergone a cloud-cloud collision. This prompts the natural suggestion that the collision is required in order to trigger the formation of the massive stars, i.e. that they would not have formed in the absence of the collision. Unfortunately, observational studies of this issue have an obvious drawback: they can only tell us what did happen, not what would have happened had the situation been different. Simulations, on the other hand, allow us to directly compare the outcome with or without a collision, or with different parameters for the collision,

enabling us to better understand the extent to which the collision actually triggers star formation.

In the work presented here, we have insufficient dynamical range to follow the formation of individual stars, and so we cannot directly address the question of whether the collision makes massive star formation more likely. However, we can explore the more general question of whether star formation overall is triggered by the collision between our simulated clouds. Here, the lesson of the simulations is somewhat mixed. It is clear from the fact that star formation occurs in our $v = 0$ control run that the cloud collision is not required in order for the clouds to begin forming stars, i.e. the collision does not trigger star formation in the sense that the clouds would otherwise remain starless. That said, the fact that star formation begins earlier in the colliding clouds and proceeds at a slightly higher rate are both indicative of the collision having a positive effect overall on the star formation efficiency of the cloud. It is possible that this enhancement of star formation would eventually be lost if we were to simulate the clouds for a much longer period. Conversely, it is also possible that the difference in efficiency would persist, particularly if the cloud lifetime is short. Ultimately, resolving this will require simulations that follow the evolution of the clouds for much longer periods and that account for the stellar feedback processes responsible for dispersing them. However, this is outside of the scope of our current study.

5 CONCLUSIONS

In this paper we presented the results of a series of simulations of the collision of two magnetised molecular clouds with mean hydrogen nuclei number densities $n \sim 80 \text{ cm}^{-3}$ embedded in a warm, diffuse intercloud medium. In our simulations, we varied the relative velocity of the clouds, the inclination of the magnetic field relative to the collision axis, and the level of Jeans refinement adopted, and investigated the impact that these variations have on the resulting star formation rate. We found that that the different conditions caused star formation to occur at different times but that once star formation had begun, the subsequent evolution of the star formation rate was very similar in all of the simulations. Colliding clouds appear to form stars at a faster rate than clouds that do not collide, suggestive of some degree of triggering of star formation, but the difference in the star formation rates is around a factor of two to three, in line with the results reported by Tanvir & Dale (2020) but much smaller than the order of magnitude increase found by Wu et al. (2017).

We further investigated the virial parameter of the cases where the collisional velocities were varied and found that the virial parameter was higher for the higher velocities. This suggests that there is more turbulence in these systems, which helps to limit the rate at which they form stars.

ACKNOWLEDGEMENTS

GHH would like to thank Elizabeth Watkins, Thomas Williams and Gerwyn Jones for their continuous help throughout this work. GHH and PCC acknowledge support from the StarFormMapper project, funded by the European Union's Horizon 2020 research and innovation programme under grant agreement No 687528. GHH, SCOG and RSK are thankful for the support from the Deutsche Forschungsgemeinschaft (DFG) via the Collaborative Research Centre (SFB 881, Project-ID 138713538) "The Milky Way System" (sub-projects

A1, B1, B2 and B8) and from the Heidelberg cluster of excellence (EXC 2181 - 390900948), "STRUCTURES: A unifying approach to emergent phenomena in the physical world, mathematics, and complex data", funded by the German Excellence Strategy. SCOG and RSK also acknowledge funding from the European Research Council in the ERC Synergy Grant "ECOGAL – Understanding our Galactic ecosystem: From the disk of the Milky Way to the formation sites of stars and planets" (project ID 855130). The project made use of computing resources provided by the state of Baden-Württemberg through bwHPC and the German Research Foundation (DFG) through grant INST 35/1134-1 FUGG. Data are stored at SDS@hd supported by the Ministry of Science, Research and the Arts Baden-Württemberg (MWK) and the German Research Foundation (DFG) through grant INST 35/1314-1 FUGG. We also thank for computing time provided by the Leibniz Computing Centre (LRZ) for project pr74nu.

Software: AREPO (Springel 2010), NUMPY (Harris et al. 2020), MATPLOTLIB (Hunter 2007), ASTROPY (Astropy Collaboration et al. 2013, 2018)

DATA AVAILABILITY

The data underlying this article will be shared on reasonable request to the corresponding author.

REFERENCES

- André P., et al., 2010, *A&A*, **518**, L102
 Anicich V. G., Huntress W. T. J., 1986, *ApJS*, **62**, 553
 Astropy Collaboration et al., 2013, *A&A*, **558**, A33
 Astropy Collaboration et al., 2018, *AJ*, **156**, 123
 Badnell N. R., 2006, *ApJS*, **167**, 334
 Badnell N. R., et al., 2003, *A&A*, **406**, 1151
 Barlow S. E., 1984, PhD thesis, UNIVERSITY OF COLORADO AT BOULDER.
 Bertelli Motta C., Clark P. C., Glover S. C. O., Klessen R. S., Pasquali A., 2016, *MNRAS*, **462**, 4171
 Blitz L., 1993, in Levy E. H., Lunine J. I., eds, *Protostars and Planets III*. p. 125
 Bruderer S., 2019, PyPDR: Python Photo Dissociation Regions (ascl:1905.027)
 Cabral B., Leedom L. C., 1993, in *Proceedings of the 20th Annual Conference on Computer Graphics and Interactive Techniques. SIGGRAPH '93*. Association for Computing Machinery, New York, NY, USA, pp 263–270, doi:10.1145/166117.166151, https://doi.org/10.1145/166117.166151
 Carty D., Goddard A., Köhler S. P. K., Sims I. R., Smith I. W. M., 2006, *Journal of Physical Chemistry A*, **110**, 3101
 Chira R. A., Beuther H., Linz H., Schuller F., Walmsley C. M., Menten K. M., Bronfman L., 2013, *A&A*, **552**, A40
 Clark P. C., Glover S. C. O., Klessen R. S., 2012, *MNRAS*, **420**, 745
 Clark P. C., Glover S. C. O., Ragan S. E., Duarte-Cabral A., 2019, *MNRAS*, **486**, 4622
 Dame T. M., Hartmann D., Thaddeus P., 2001, *ApJ*, **547**, 792
 Dedner A., Kemm F., Kröner D., Munz C.-D., Schnitzer T., Wesenberg M., 2002, *Journal of Computational Physics*, **175**, 645
 Dobbs C. L., Pringle J. E., Duarte-Cabral A., 2015, *MNRAS*, **446**, 3608
 Draine B. T., 1978, *ApJS*, **36**, 595
 Ferland G. J., Peterson B. M., Horne K., Welsh W. F., Nahar S. N., 1992, *ApJ*, **387**, 95
 Ferland G. J., Korista K. T., Verner D. A., Ferguson J. W., Kingdon J. B., Verner E. M., 1998, *PASP*, **110**, 761
 Fujita S., et al., 2021, *PASJ*, **73**, S201
 Fukui Y., et al., 1999, *PASJ*, **51**, 745

- Fukui Y., Tsuge K., Sano H., Bekki K., Yozin C., Tachihara K., Inoue T., 2017, *PASJ*, **69**, L5
- Fukui Y., et al., 2019, *ApJ*, **886**, 14
- Fukui Y., Habe A., Inoue T., Enokiya R., Tachihara K., 2021, *PASJ*, **73**, S1
- Geppert W. D., et al., 2005, in *Journal of Physics Conference Series*. pp 26–31, doi:10.1088/1742-6596/4/1/004
- Glassgold A. E., Langer W. D., 1974, *ApJ*, **193**, 73
- Glover S. C. O., Clark P. C., 2012, *MNRAS*, **421**, 116
- Glover S. C. O., Jappsen A. K., 2007, *ApJ*, **666**, 1
- Glover S. C. O., Federrath C., Mac Low M. M., Klessen R. S., 2010, *MNRAS*, **404**, 2
- Gong M., Ostriker E. C., Wolfire M. G., 2017, *ApJ*, **843**, 38
- Habe A., Ohta K., 1992, *PASJ*, **44**, 203
- Habing H. J., 1968, *Bull. Astron. Inst. Netherlands*, **19**, 421
- Harris C. R., et al., 2020, *Nature*, **585**, 357
- Heays A. N., Bosman A. D., van Dishoeck E. F., 2017, *A&A*, **602**, A105
- Hollenbach D., McKee C. F., 1979, *ApJS*, **41**, 555
- Hummer D. G., Storey P. J., 1998, *MNRAS*, **297**, 1073
- Hunter J. D., 2007, *Computing in Science & Engineering*, **9**, 90
- Jacobs T. A., Giedt R. R., Cohen N., 1967, *J. Chem. Phys.*, **47**, 54
- Janev R. K., Langer W. D., Evans K., 1987, *Elementary processes in Hydrogen-Helium plasmas - Cross sections and reaction rate coefficients*. Springer
- Karpas Z., Anicich V., Huntress W. T., 1979, *J. Chem. Phys.*, **70**, 2877
- Kim J. K., Theard L. P., Huntress W. T. J., 1975, *Chemical Physics Letters*, **32**, 610
- Krumholz M. R., McKee C. F., 2005, *ApJ*, **630**, 250
- Lepp S., Shull J. M., 1983, *ApJ*, **270**, 578
- Leroy A. K., et al., 2021, arXiv e-prints, p. arXiv:2104.07739
- Linder F., Janev R. K., Botero J., 1995, in Janev R. K., ed., *Atomic and Molecular Processes in Fusion Edge Plasmas*. p. 397
- Mac Low M. M., Shull J. M., 1986, *ApJ*, **302**, 585
- Martin P. G., Schwarz D. H., Mandy M. E., 1996, *ApJ*, **461**, 265
- Martin P. G., Keogh W. J., Mandy M. E., 1998, *ApJ*, **499**, 793
- McCall B. J., et al., 2004, *Phys. Rev. A*, **70**, 052716
- McElroy D., Walsh C., Markwick A. J., Cordiner M. A., Smith K., Millar T. J., 2013, *A&A*, **550**, A36
- McKinnon R., Torrey P., Vogelsberger M., Hayward C. C., Marinacci F., 2017, *MNRAS*, **468**, 1505
- Mitchell G. F., 1984, *ApJS*, **54**, 81
- Motte F., Bontemps S., Louvet F., 2018, *ARA&A*, **56**, 41
- Nahar S. N., 2000, *ApJS*, **126**, 537
- Neelamkoda N., Tokuda K., Barman S., Kondo H., Sano H., Onishi T., 2021, *ApJ*, **908**, L43
- Nelson R. P., Langer W. D., 1999, *ApJ*, **524**, 923
- Osterbrock D. E., 1989, *Astrophysics of gaseous nebulae and active galactic nuclei*. University Science Books
- Pakmor R., Springel V., 2013, *MNRAS*, **432**, 176
- Pequignot D., Aldrovandi S. M. V., 1986, *A&A*, **161**, 169
- Petuchowski S. J., Dwek E., Allen J. E. J., Nuth J. A. I., 1989, *ApJ*, **342**, 406
- Powell K. G., Roe P. L., Linde T. J., Gombosi T. I., De Zeeuw D. L., 1999, *J. Comp. Phys.*, **154**, 284
- Prasad S. S., Huntress W. T. J., 1980, *ApJS*, **43**, 1
- Roman-Duval J., Jackson J. M., Heyer M., Rathborne J., Simon R., 2010, *ApJ*, **723**, 492
- Scoville N. Z., Sanders D. B., Clemens D. P., 1986, *ApJ*, **310**, L77
- Sembach K. R., Howk J. C., Ryans R. S. I., Keenan F. P., 2000, *ApJ*, **528**, 310
- Shapiro P. R., Kang H., 1987, *ApJ*, **318**, 32
- Smith B. D., et al., 2017, *MNRAS*, **466**, 2217
- Sormani M. C., et al., 2019, *MNRAS*, **488**, 4663
- Springel V., 2005, *MNRAS*, **364**, 1105
- Springel V., 2010, *MNRAS*, **401**, 791
- Stancil P. C., Lepp S., Dalgarno A., 1998, *ApJ*, **509**, 1
- Stancil P. C., Schultz D. R., Kimura M., Gu J. P., Hirsch G., Buenker R. J., 1999, *A&AS*, **140**, 225
- Tan J. C., Beltrán M. T., Caselli P., Fontani F., Fuente A., Krumholz M. R., McKee C. F., Stolte A., 2014, in Beuther H., Klessen R. S., Dullemond C. P., Henning T., eds, *Protostars and Planets VI*. p. 149 (arXiv:1402.0919), doi:10.2458/azu_uapress_9780816531240-ch007
- Tanvir T. S., Dale J. E., 2020, *MNRAS*, **494**, 246
- Tasker E. J., Tan J. C., 2009, *ApJ*, **700**, 358
- Tokuda K., et al., 2019, *ApJ*, **886**, 15
- Tress R. G., Smith R. J., Sormani M. C., Glover S. C. O., Klessen R. S., Mac Low M.-M., Clark P. C., 2020, *MNRAS*, **492**, 2973
- Trevisan C. S., Tennyson J., 2002, *Plasma Physics and Controlled Fusion*, **44**, 1263
- Tsang W., Hampson R. F., 1986, *Journal of Physical and Chemical Reference Data*, **15**, 1087
- Vissapragada S., Buzard C. F., Miller K. A., O'Connor A. P., de Ruetten N., Urbain X., Savin D. W., 2016, *ApJ*, **832**, 31
- Voronov G. S., 1997, *Atomic Data and Nuclear Data Tables*, **65**, 1
- Wakelam V., et al., 2010, *Space Sci. Rev.*, **156**, 13
- Wareing C. J., Pittard J. M., Falle S. A. E. G., 2017, *MNRAS*, **470**, 2283
- Weingartner J. C., Draine B. T., 2001, *ApJ*, **563**, 842
- Wolfire M. G., Tielens A. G. G. M., Hollenbach D., Kaufman M. J., 2008, *ApJ*, **680**, 384
- Wu B., Van Loo S., Tan J. C., Bruderer S., 2015, *ApJ*, **811**, 56
- Wu B., Tan J. C., Christie D., Nakamura F., Van Loo S., Collins D., 2017, *ApJ*, **841**, 88
- Zanchet A., Bussery-Honvault B., Jorfi M., Honvault P., 2009, *Physical Chemistry Chemical Physics (Incorporating Faraday Transactions)*, **11**, 6182
- de Ruetten N., Miller K. A., O'Connor A. P., Urbain X., Buzard C. F., Vissapragada S., Savin D. W., 2016, *ApJ*, **816**, 31
- van Dishoeck E. F., 1988, in Millar T. J., Williams D. A., eds, , Vol. 146, *Rate Coefficients in Astrochemistry*. Kluwer, p. 49, doi:10.1007/978-94-009-3007-0_4

APPENDIX A: CHEMICAL NETWORK

The reactions included in our chemical network are summarized in Tables A1 and A2. Our network is based on the one presented by Gong et al. (2017; hereafter, G17), but also includes several reactions not included in their network, denoted in the tables as “Not in G17”. In addition, for some reactions we have adopted a different rate coefficient from the one listed in G17; these are also indicated in the Table, with the note “Different rate”. Reactions with no attached note are treated exactly the same as in G17. Below, we discuss the rationale for the differences between our network and the original G17 network. For the most part, these differences are to make the network more robust when applied to physical conditions outside of the range considered by G17 and have little impact on its behaviour in the typical photodissociation region (PDR) conditions that were the main focus of their study.

Reactions in our network that are not in G17

Reactions 5, 12, 19 & 40

These reactions – the collisional dissociation of H₂ by electrons and the collisional ionisation of He, C and Si – were neglected by G17 because they are unimportant at typical PDR temperatures. However, they can become important in hot shocked gas with $T \gg 10^4$ K and we include them to ensure that the chemical network behaves reasonably at these high temperatures.

Reaction 16

The formation of CH_x – a pseudo-molecule that represents light hydrocarbons such as CH, CH₂, CH⁺ etc. – by radiative associa-

Table A1. List of collisional chemical reactions included in our chemical network

No.	Reaction	Notes	Refs.
1	$H + e^- \rightarrow H^+ + e^- + e^-$		1
2	$H^+ + e \rightarrow H + \gamma$		2
3	$He^+ + H_2 \rightarrow H_2^+ + He$		3
4	$He^+ + H_2 \rightarrow H^+ + H + He$		3
5	$H_2 + e^- \rightarrow H + H + e^-$	Not in G17	4
6	$H_2 + H \rightarrow H + H + H$	Different rate	5, 6, 7
7	$H_2 + H_2 \rightarrow H + H + H_2$	Different rate	8, 9
8	$H_2^+ + H_2 \rightarrow H_3^+ + H$	Different rate	10
9	$H_2^+ + H \rightarrow H_2 + H^+$		11
10	$H_3^+ + e^- \rightarrow H + H + H$		12
11	$H_3^+ + e^- \rightarrow H_2 + H$		12
12	$He + e^- \rightarrow He^+ + e^- + e^-$	Not in G17	1
13	$He^+ + e^- \rightarrow He + \gamma$	Different rate	13, 14
14	$C^+ + H_2 \rightarrow CH_x + H$		15, 16
15	$C^+ + H_2 + e^- \rightarrow C + H + H$		15, 16
16	$C + H_2 \rightarrow CH_x + \gamma$	Not in G17	17
17	$C + H_3^+ \rightarrow CH_x + H_2$		18
18	$C^+ + e^- \rightarrow C + \gamma$	Different rate	14, 19
19	$C + e^- \rightarrow C^+ + e^- + e^-$	Not in G17	20
20	$O^+ + H \rightarrow O + H^+$		21
21	$O + H^+ \rightarrow O^+ + H$		21
22	$O^+ + H_2 \rightarrow OH_x + H$		16
23	$O^+ + H_2 + e \rightarrow O + H + H$		16
24	$O + H_3^+ \rightarrow OH_x + H_2$		22
25	$O + H_3^+ + e^- \rightarrow H_2 + O + H$		22
26	$C^+ + OH_x \rightarrow HCO^+$		16
27	$C + OH_x \rightarrow CO + H$		23
28	$CH_x + He^+ \rightarrow C^+ + He + H$	Not in G17	17, 24
29	$CH_x + H \rightarrow H_2 + C$		15
30	$CH_x + O \rightarrow CO + H$		15
31	$OH_x + H \rightarrow O + H_2$	Not in G17	24, 25
32	$OH_x + O \rightarrow O + O + H$		26
33	$OH_x + He^+ \rightarrow O^+ + He + H$		15
34	$CO + H_3^+ \rightarrow HCO^+ + H_2$		27
35	$CO + He^+ \rightarrow C^+ + O + He$	Different rate	28
36	$CO + H \rightarrow C + OH_x$	Not in G17	29
37	$HCO^+ + e^- \rightarrow OH_x + C$	Not in G17	30
38	$HCO^+ + e^- \rightarrow CO + H$		30
39	$Si^+ + e^- \rightarrow Si + \gamma$	Different rate	31
40	$Si + e^- \rightarrow Si^+ + e^- + e^-$	Not in G17	20

References: 1: Janev et al. (1987); 2: Ferland et al. (1992); 3: Barlow (1984); 4: Trevisan & Tennyson (2002); 5: Mac Low & Shull (1986); 6: Lepp & Shull (1983); 7: Martin et al. (1996); 8: Martin et al. (1998); 9: Jacobs et al. (1967); 10: Linder et al. (1995); 11: Karpas et al. (1979); 12: McCall et al. (2004); 13: Hummer & Storey (1998); 14: Badnell (2006); 15: Wakelam et al. (2010); 16: Gong et al. (2017); 17: Prasad & Huntress (1980); 18: Vissapragada et al. (2016); 19: Badnell et al. (2003); 20: Voronov (1997); 21: Stancil et al. (1999); 22: Fit by G17 to de Ruelle et al. (2016); 23: Zanchet et al. (2009); 24: McElroy et al. (2013); 25: Tsang & Hampson (1986); 26: Carty et al. (2006); 27: Kim et al. (1975); 28: Petuchowski et al. (1989); 29: Mitchell (1984); 30: Geppert et al. (2005); 31: Nahar (2000);

tion of atomic carbon and H_2 is neglected by G17 because it is a slow process and in typical Milky Way conditions is unimportant compared to CH_x formation via the reaction of C and H_3^+ (reaction 17). However, the abundance of H_3^+ , and hence the rate of reaction 17, depends sensitively on the cosmic ray ionisation rate, and so reaction 16 can become important in conditions where this is much smaller than the typical Milky Way value.

Table A2. List of grain surface, cosmic ray and photochemical reactions included in our chemical network

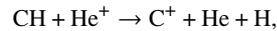
No.	Reaction	Notes	Refs.
41	$H + H + gr \rightarrow H_2 + gr$	Different rate	1
42	$H^+ + e^- + gr \rightarrow H + gr$	Different rate	2
43	$C^+ + e^- + gr \rightarrow C + gr$	Different rate	2
44	$He^+ + e^- + gr \rightarrow He + gr$	Different rate	2
45	$Si^+ + e^- + gr \rightarrow Si + gr$	Different rate	2
46	$H + cr \rightarrow H^+ + e^-$		3
47	$H_2 + cr \rightarrow H_2^+ + e^-$		3
48	$H_2 + cr \rightarrow H + H^+ + e^-$	Not in G17	4
49	$H_2 + cr \rightarrow H + H$	Not in G17	4
50	$He + cr \rightarrow He^+ + e^-$		4
51	$C + cr \rightarrow C^+ + e^-$		4
52	$CO + cr + H \rightarrow HCO^+ + e^-$		5
53	$C + \gamma_{cr} \rightarrow C^+ + e^-$		6
54	$CO + \gamma_{cr} \rightarrow C^+ + e^-$		6
55	$Si + \gamma_{cr} \rightarrow Si^+ + e^-$		6
56	$C + \gamma \rightarrow C^+ + e^-$		6
57	$CH_x + \gamma \rightarrow C + H$		5,6
58	$CO + \gamma \rightarrow C + O$		6
59	$OH_x + \gamma \rightarrow O + H$		5,6
60	$Si + \gamma \rightarrow Si^+ + e^-$		7
61	$H_2 + \gamma \rightarrow H + H$		8

The primary cosmic ray ionization rate of atomic hydrogen is a free parameter in our chemical model and the value we select for this in our simulations is discussed in the main text. The total (primary plus secondary) rate for H (reaction 46), as well as the total cosmic ray ionization rates of H_2 , He, C, CO and Si (reactions 47–55) are scaled relative to this value using scaling factors derived from the cited references.

References: 1: Hollenbach & McKee (1979); 2: Weingartner & Draine (2001), modified as described in the text; 3: Glassgold & Langer (1974); 4: McElroy et al. (2013); 5: Gong et al. (2017); 6: Heays et al. (2017); 7: van Dishoeck (1988); 8: 1996ApJ...468..269D

Reaction 28

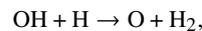
In neutral gas, this reaction is unimportant compared to reaction 29. It is included here to ensure that an appropriate loss route exists for CH_x in very highly ionized gas. For the rate coefficient, we use the value given by McElroy et al. (2013) for the reaction



which comes originally from Prasad & Huntress (1980).

Reaction 31

This reaction is unimportant compared to reaction 32 at temperatures lower than 500 K, but quickly becomes dominant at higher temperatures, given a sufficient supply of hydrogen atoms. It is therefore not important in typical PDR conditions but can become important in shocks. For the rate coefficient, we adopt the value given by McElroy et al. (2013) for the reaction



which is based on Tsang & Hampson (1986).

Reaction 36

This reaction has a substantial activation energy ($E/k \sim 78000$ K) and is therefore unimportant in typical PDR conditions. However,

it can become important in hot, shocked gas. In particular, we have found that if strong shocks occur in gas with high A_V , CO can persist in the gas up to artificially high temperatures of $> 10^4$ K if this reaction is not included.

Reaction 37

As G17 note in their appendix A, the destruction of HCO^+ is dominated by the reaction $\text{HCO}^+ + e^- \rightarrow \text{CO} + \text{H}$ (reaction 38 above). However, although CO and H are the most likely products of the dissociative recombination of HCO^+ , roughly 8% of the time this process instead yields C and OH (Geppert et al. 2005). We include this outcome here for completeness.

Reactions 48 & 49

Although interactions between high energy cosmic rays and H_2 molecules primarily produce H_2^+ ions (reaction 47), a small fraction of the time the outcome can instead be a hydrogen atom, a proton and an electron (reaction 48) or two hydrogen atoms (reaction 49). These outcomes were neglected by G17 but we include them here for completeness.

Reactions with different rate coefficients

Reactions 6 & 7

We use the same low density limits for the rates of these reactions as in G17, and the same expression for the H_2 critical density. However, we use slightly different expressions for the high density limits: G17 follow Lepp & Shull (1983) and Shapiro & Kang (1987) for reactions 6 and 7, respectively, whereas we use the expression given by Martin et al. (1996) for the high density limit of reaction 6 and adopt a value 8 times smaller than this for reaction 7, following Jacobs et al. (1967). At densities below the H_2 critical density ($n \sim 10^4 \text{ cm}^{-3}$), we therefore recover the same behaviour as in G17, and we also find good agreement between the different treatments in hot ($T > 6000$ K), high density gas. The only significant difference comes in cool dense gas, where the Lepp & Shull (1983) expression over-estimates the H_2 collisional dissociation rate. However, given the small size of this rate at these temperatures, this difference is likely only of minor importance.

Reaction 8

We adopt the rate coefficient for this reaction given in Stancil et al. (1998), which is their fit to cross-section data from Linder et al. (1995). G17 also cite Linder et al. (1995) as the source of their rate coefficient, but their expression is $\sim 27\%$ larger than the one given in Stancil et al. (1998). The source of this discrepancy is unclear. However, in practice it is unlikely to be important as this reaction is never the rate-limiting step for the formation of H_3^+ .

Reaction 13

G17 assume case B for the radiative recombination of He^+ and use a reaction rate coefficient from Glover et al. (2010) that is a fit to the values tabulated by Hummer & Storey (1998). Our treatment differs from this in two respects. First, in addition to radiative recombination, we also account for dielectronic recombination of He^+ , using a rate coefficient from Badnell (2006). Second, although we assume

the on-the-spot approximation applies, we do not assume pure case B recombination for He^+ , which would be valid only in a gas consisting of pure helium. Instead, we follow Osterbrock (1989) and account for the fact that some of the photons produced during the recombination of He^+ are absorbed by atomic hydrogen rather than He. (A more detailed discussion of how this is done can be found in Glover & Jappsen 2007).

Reaction 18

As in G17, we adopt a rate coefficient for C^+ recombination that is the sum of two contributions: one corresponding to radiative recombination, taken from Badnell (2006), and one corresponding to dielectronic recombination, taken from Badnell et al. (2003). In the expression that they use for the dielectronic recombination rate, G17 retain only the first three terms, which is sufficient at low temperatures but which leads to inaccuracies at high temperatures ($T \gg 10^4$ K). In our implementation of this rate, we instead retain all of the terms from the expression given by Badnell et al. (2003).

Reaction 35

G17 adopt a temperature-independent rate for this reaction from Anicich & Huntress (1986), whereas we adopt the temperature-dependent value proposed by Petuchowski et al. (1989). In practice, there is very little difference between these two values at typical PDR temperatures.

Reaction 39

G17 adopt a rate coefficient for this reaction that they credit to McElroy et al. (2013) but that derives originally from Pequignot & Aldrovandi (1986). However, this fit is formally valid only in the temperature range $10 < T < 1000$ K. Moreover, it only accounts for the contribution from radiative recombination, and not the dielectronic recombination term that dominates at high temperatures. We adopt instead a rate from Nahar (2000) that accounts for both processes.

Reaction 41

G17 adopt a constant value of $3 \times 10^{-17} \text{ cm}^3 \text{ s}^{-1}$ for the rate coefficient for this reaction. We instead adopt the rate coefficient given in Hollenbach & McKee (1979), which depends on the temperatures of both the gas and the dust grains.

Reaction 42–45

We follow G17 in that we use the reaction rate coefficients given in Weingartner & Draine (2001) for the recombination of H^+ , C^+ , He^+ and Si^+ ions on grain surfaces (reactions 42–45), multiplied by a factor of 0.6 to better match the results of Wolfire et al. (2008). These rate coefficients depend primarily on the parameter

$$\psi = \frac{G\sqrt{T}}{n_e}, \quad (\text{A1})$$

where G is the local value of the interstellar radiation field in Habing (1968) units and n_e is the electron number density. One important way in which our treatment differs from G17 is in our treatment of these rate coefficients for low values of ψ . The expressions given in Weingartner & Draine (2001) are stated to be valid only for

$\psi > 100 \text{ K}^{1/2} \text{ cm}^3$ and applying them unaltered when the value of ψ is smaller than this yields recombination rates that are significant over-estimates of the true values. To avoid this, we simply assume that the rates in gas with $\psi < 100 \text{ K}^{1/2} \text{ cm}^3$ are the same as those in gas with $\psi = 100 \text{ K}^{1/2} \text{ cm}^3$ (c.f. figure 3 in Weingartner & Draine 2001).

The other main difference between our treatment and that in G17 is that we multiply the grain surface recombination rates by an additional factor of $\exp(-T/34000)$. This is to ensure that the recombination rates fall rapidly to zero in very hot gas, in conditions where we expect that in reality the dust would be quickly destroyed by sputtering. This modification would not be necessary if we were using a more sophisticated treatment of dust evolution that accounted for this effect (see e.g. McKinnon et al. 2017), but this is a topic for future work.

APPENDIX B: POST-COLLISION MAGNETIC FIELD

Here we illustrate how the magnetic field is warped in the process of the collision of the clouds. Figures B1 & B2 show images of the magnitude and z -component of the magnetic field, respectively, which have been convolved with the x - y components of magnetic field via line integral convolution (LIC) (Cabral & Leedom 1993). This is done to give indication of the direction of the magnetic field in the x - y plane.

We noted in Section 3.1 that an early onset of star formation is observed for a magnetic field inclination of $\theta = 0$, i.e. a field that is initially parallel to the collision axis. In this case, the magnetic field is not compressed during the collision and hence does not hinder the collision process. This can be seen clearly in the central panels of Figures B1 & B2, where the pattern of the map generated by the LIC lies predominantly parallel to the x -axis. Only at the site of the collision is the magnetic field distorted, owing to the local collapse of the gas.

This paper has been typeset from a $\text{\TeX}/\text{\LaTeX}$ file prepared by the author.

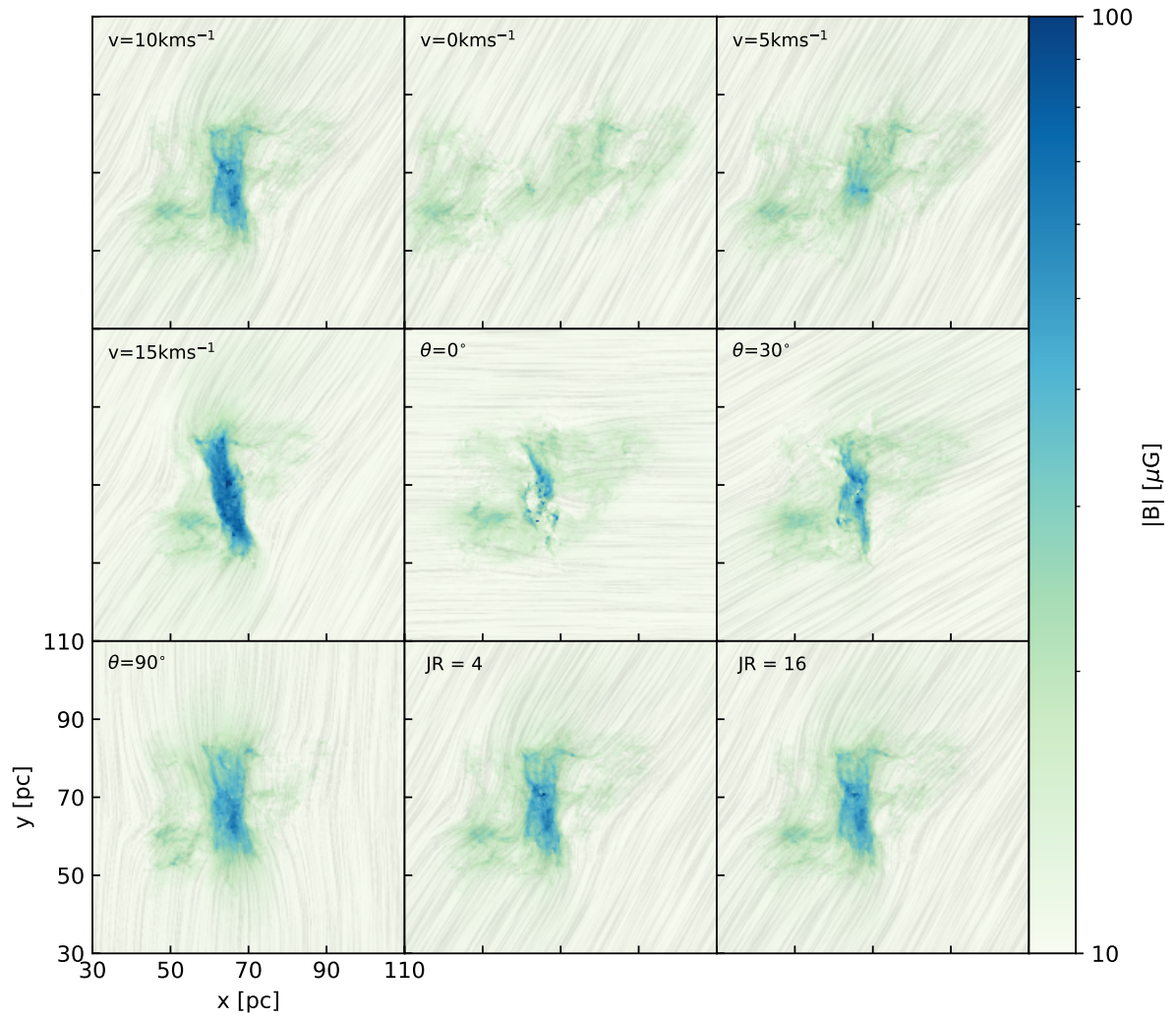


Figure B1. Maps of the magnetic field strength of the simulations carried out at $t = 2.40$ Myr. Line integral convolution (LIC) is used on the map to indicate the direction of the magnetic field in the x - y plane.

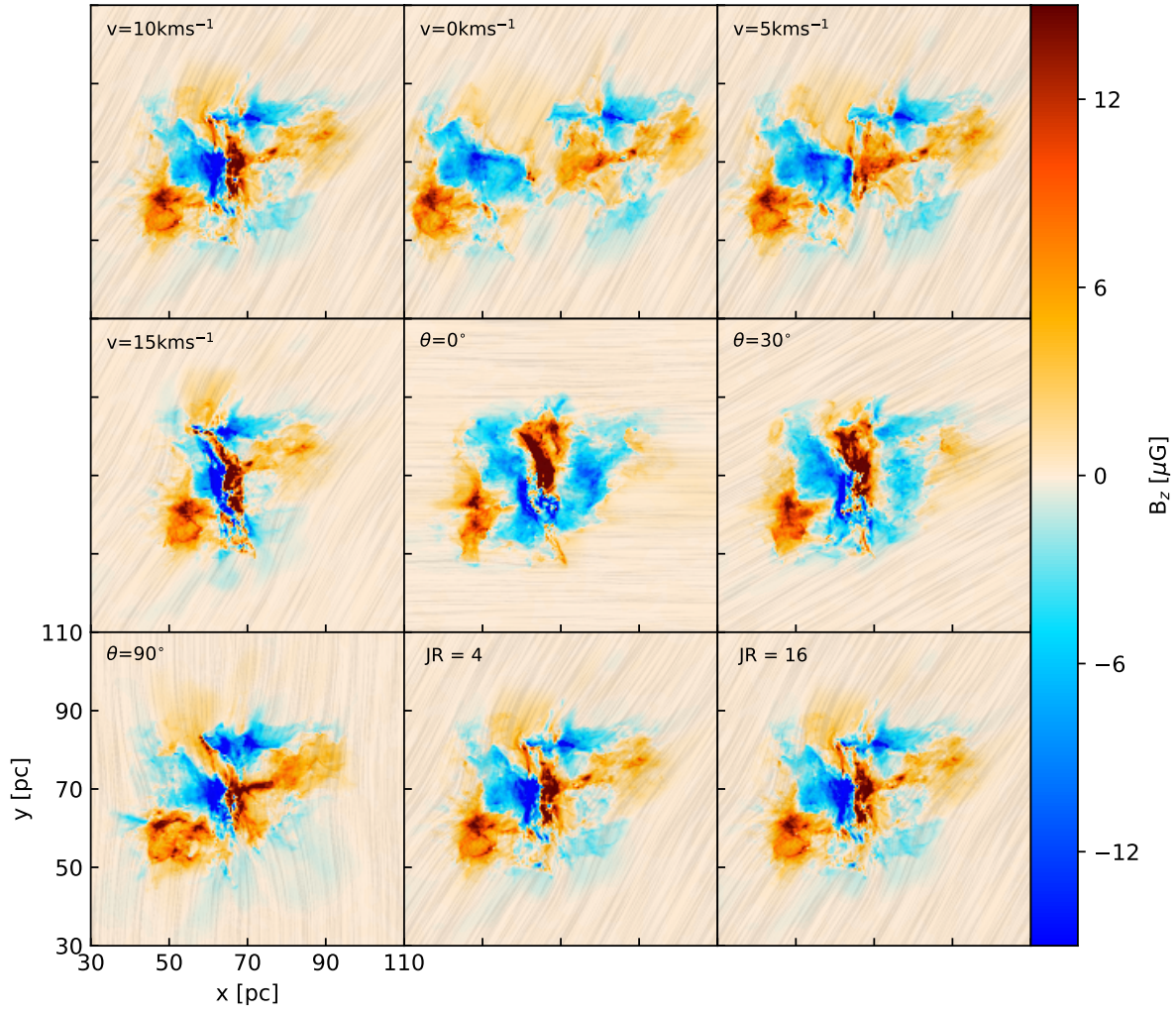


Figure B2. Same as figure B1 but for the z component of the magnetic field